Nighttime cirrus detection using Atmospheric Infrared Sounder window channels and total column water vapor

Brian H. Kahn,[1,2] Kuo Nan Liou,[2] Sung-Yung Lee,[1] Evan F. Fishbein,[1] Sergio DeSouza-Machado,[3] Annmarie Eldering,[1,2] Eric J. Fetzer,[1] Scott E. Hannon,[3] and L. Larrabee Strow[3]

Received 8 September 2004; revised 7 December 2004; accepted 29 December 2004; published 2 April 2005.

[1] A method of cirrus detection at nighttime is presented that utilizes 3.8 and 10.4 μm infrared (IR) window brightness temperature differences (dBT) and total column precipitable water (PW) measurements. This technique is applied to the Atmospheric Infrared Sounder (AIRS) and Advanced Microwave Sounding Unit A (AMSU-A) instrument suite on board EOS-Aqua, where dBT is determined from sets of carefully selected AIRS window channels, while PW is derived from the synergistic AIRS and AMSU-A water vapor retrievals. Simulated and observed dBT for a particular value of PW are not constant; several physical factors impact dBT, including the variability in temperature and relative humidity profiles, surface emissivity, instrument noise, and skin/near-surface air temperature differences. We simulate clear-sky dBT over a realistic range of PWs using 8350 radiosondes that have varying temperature and relative humidity profiles. Thresholds between cloudy and uncertain sky conditions are derived once the scatter in the clear-sky dBT is determined. Simulations of optically thin cirrus indicate that this technique is most sensitive to cirrus optical depth in the 10 μm window of 0.1–0.15 or greater over the tropical and subtropical oceans, where surface emissivity and skin/near-surface air temperature impacts on the IR radiances are minimal. The method at present is generally valid over oceanic regions only, specifically, the tropics and subtropics. The detection of thin cirrus, and other cloud types, is validated using observations at the Atmospheric Radiation Measurement (ARM) program site located at Manus Island in the tropical western Pacific for 89 coincident EOS-Aqua overpasses. Even though the emphasis of this work is on the detection of thin cirrus at nighttime, this technique is sensitive to a broad cloud morphology. The cloud detection technique agrees with ARM-detected clouds 82–84% of the time, which include thin cirrus, as well as other cloud types. Most of the disagreements are well explained by AIRS footprint-scale heterogeneity compared to ARM point measurements, cirrus overlying lower-layer water clouds, possible mixed phase microphysics in midlevel clouds, and significant IR channel noise for cold BT scenes over deep convective towers.

Citation: Kahn, B. H., K. N. Liou, S.-Y. Lee, E. F. Fishbein, S. DeSouza-Machado, A. Eldering, E. J. Fetzer, S. E. Hannon, and L. L. Strow (2005), Nighttime cirrus detection using Atmospheric Infrared Sounder window channels and total column water vapor, *J. Geophys. Res.*, *110*, D07203, doi:10.1029/2004JD005430.

1. Introduction

[2] An extensive body of scientific literature reveals the importance of the role that cirrus plays in regulating Earth's radiative balance [*Liou*, 1986; *Stephens*, 2002; *Garrett et al.*, 2003], the dehydration of the tropical transition layer and lower stratosphere [*Holton and Gettelman*, 2001; *Sherwood and Dessler*, 2001; *Jensen and Pfister*, 2004], the maintenance of the hydrological cycle [*Webster*, 1994], and the interaction with upper tropospheric chemical processes [*Gao et al.*, 2003; *Ziereis et al.*, 2004]. Accurate global observations of cirrus at high spatial and temporal resolution are necessary to improve our basic understanding of these clouds. Such observations would include their microphysical and bulk properties, spatial structure and temporal distributions, as well as their interaction with the atmospheric circulation through radiative and thermodynamic effects [*Stephens*, 2002]. The synergistic use of the voluminous spaceborne "A-train" observations [*Stephens et al.*, 2002], along with surface-based lidar and cloud radar, and airborne in situ measurements is a significant step in expanding our knowledge and understanding of cirrus.

[1]Jet Propulsion Laboratory, Pasadena, California, USA.
[2]Department of Atmospheric and Oceanic Sciences, University of California, Los Angeles, California, USA.
[3]Department of Physics, University of Maryland Baltimore, Baltimore, Maryland, USA.

Copyright 2005 by the American Geophysical Union.
0148-0227/05/2004JD005430$09.00

[3] Some of the largest uncertainties in forecasting future climate change based on numerical models are a direct consequence of our inadequate knowledge about cloud processes [*Randall et al.*, 2003]. Comparisons of observed and simulated cloud properties from several general circulation models (GCMs) have shown mixed results. In a comprehensive analysis, *Potter and Cess* [2004] showed many GCMs used for climate analysis have significant biases of net cloud radiative forcing (CRF) when simulating the present-day climate. When regionally averaged net CRF biases are small, further analysis shows the agreement is often the result of compensating model errors in cloud height, cloud fraction, and optical depth.

[4] The first step in retrieving cirrus properties is the identification of cirrus within a given measurement. There are numerous cirrus detection techniques applied to a wide range of surface, airborne, and spaceborne instrument platforms and geometries that use measurements at a large assortment of wavelengths throughout the solar and terrestrial spectra [*Ackerman et al.*, 1998; *Rolland et al.*, 2000; *Rolland and Liou*, 2001; *Ou et al.*, 2003]; different channel combinations are sensitive to particular ranges in optical depth, cloud height and thickness, effective radius (r_e), particle shape, habit, and orientation. Numerous surface-based, in situ, and satellite observations have shown an extensive amount of optically tenuous cirrus, especially in the tropics [*Prabhakara et al.*, 1988, 1993; *Platt et al.*, 1998; *Wylie and Menzel*, 1999; *McFarquhar et al.*, 2000; *Comstock et al.*, 2002; *Peter et al.*, 2003].

[5] By using a combination of the 10 μm IR split window and 1.38 μm channels, *Roskovensky and Liou* [2003] demonstrated that the Moderate Resolution Imaging Spectroradiometer (MODIS) [*Platnick et al.*, 2003] is capable of retrieving cirrus as tenuous as $\tau_{VIS} \sim 0.1$. *Dessler and Yang* [2003] suggested that the MODIS-Terra 1.38 μm band has the capability to detect borderline subvisual cirrus with $\tau_{VIS} \geq 0.02-0.04$ over water surfaces, as demonstrated in pixels that have been flagged as cloud free by the MODIS cloud mask at the 99% probability–clear level. Unfortunately, at night the 1.38 μm band cannot be utilized because there is no reflected solar radiation; thus the focus for nighttime cirrus detection must remain on radiance in the thermal emission spectrum. In this work, we will focus strictly on thermal emission measurements made from the AIRS for the purposes of cirrus detection at night, which compliments the capabilities of the daytime 1.38 μm MODIS band.

[6] The traditional split window and trispectral techniques (which use BT differences between two or three channels in the 8–12 μm window region) for cloud identification and categorization have been widely used for many years as stand-alone methods, or combined with other channels, or independent sources of data [e.g., *Inoue*, 1985; *Strabala et al.*, 1994]. However, there is a greater sensitivity in the IR radiance spectrum between "shortwave" (e.g., 3.7 μm) and "longwave" (8–12 μm) window channels over the more traditional split window method for relatively thin cirrus and other cloud types [*Lutz et al.*, 2003]. For many years, researchers have used shortwave and longwave channel combinations for retrieving cirrus [*Ou et al.*, 1995; *Baran et al.*, 1999], stratus [*Lee et al.*, 1997], and multilayered cloud properties containing both cirrus and stratus [*Baum et al.*, 2003].

[7] One of the fundamental problems in the identification and retrieval of cirrus properties using a simple difference (dBT) between two (or more) channels is the fact that the dBT is a function of both the cirrus itself and other physical factors. *Kahn et al.* [2004] show the thermal IR spectrum has a similar sensitivity to changes in values of many cirrus properties (IWP, cloud height and thickness, r_e, size distribution), as well as atmospheric temperature and humidity profiles. Other studies have shown that distinct spectral shapes on mid IR radiances can result from volcanic aerosol [*Ackerman and Strabala*, 1994; *Baran and Foot*, 1994] and mineral dust [*Pierangelo et al.*, 2004] loading. One way to constrain the "parameter space" is by using independent observations of the total water vapor path [*Saunders and Kriebel*, 1988; *Hutchison et al.*, 1995; *Hutchison and Hardy*, 1995; *Platt et al.*, 1998].

[8] In this work, we developed a thin cirrus detection technique on the basis of a number of carefully selected 3.8 and 10.4 μm window channels in the Atmospheric Infrared Sounder (AIRS) spectrum and the PW determined from the combined use of the Advanced Microwave Sounding Unit A (AMSU-A) and AIRS, colocated onboard EOS-Aqua [*Aumann et al.*, 2003]. AIRS is an IR spectrometer spanning the thermal emission spectrum from 3.7–15.4 μm that scans ±48.95° of nadir. The spectral resolution is nominally $\lambda/\Delta\lambda = 1200$, with a footprint diameter of 13.5 km at nadir view. AMSU-A is primarily a temperature sounder, but is capable of deriving total column PW [*Lambrigtsen*, 2003]. AMSU-A and AIRS are used synergistically to retrieve temperature and humidity profiles [*Susskind et al.*, 2003]; the total column PW is derived from the sum of the vertical layers in the retrieved humidity profile. Despite the coarser spatial resolution of AIRS compared to platforms such as the advanced very high resolution radiometer (AVHRR) and MODIS, the spectral resolution is much higher for AIRS; window channels in between absorption lines are easily selected, and as a result, the effect of the water vapor continuum can be isolated from the absorption lines. The colocation of AMSU-A and AIRS aboard EOS-Aqua makes this method a practical nighttime cirrus detection technique for operational purposes.

2. Methodology

[9] The AIRS channels selected in this work met the following criteria: (1) there is a minimum of contamination from gaseous absorption lines, (2) there is a minimum of noise equivalent delta temperature (NEdT), and (3) one channel must be located in the shortwave 3.7–3.9 μm region and the other somewhere in the 8–12 μm window to maximize the spectral signature of cirrus over that of a traditional split window difference. The reasoning behind criterion 1 is that gases including H_2O, CO_2, O_3, CH_4, and N_2O may cause a reduction in the upwelling transmittance, more so in particular spectral regions than others. The absorption lines can be accounted for in the simulations; however, this requires accurate gas and temperature profile information, which is not available for every AIRS measurement. Thus avoiding these channels is the easiest way of circumventing this problem, and we are left with accounting for the H_2O continuum. After consideration of these points, we selected an average of channels 902

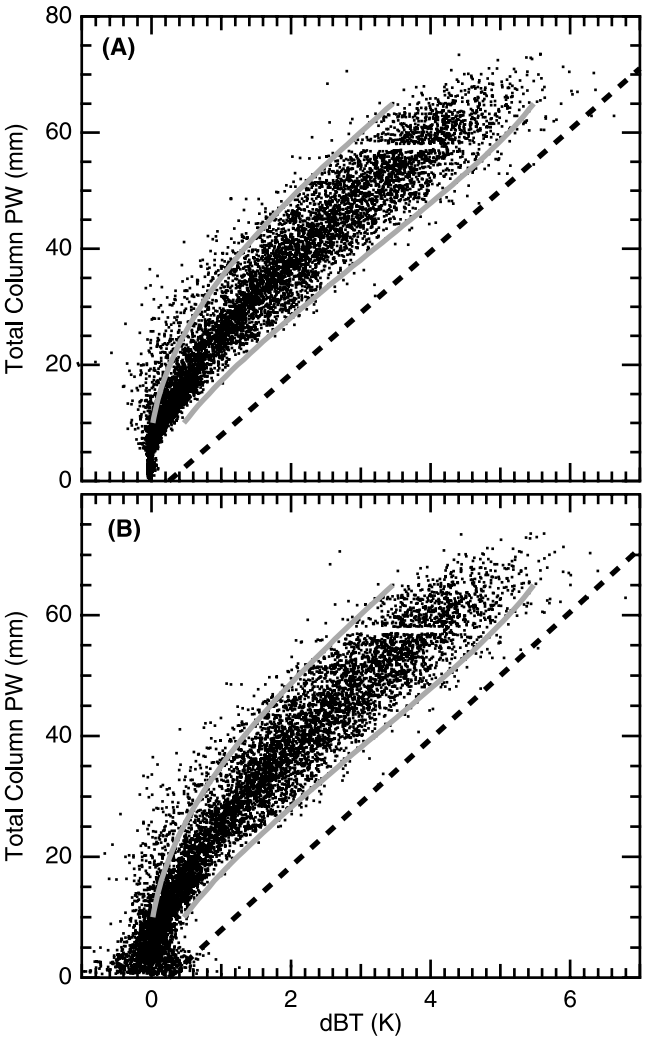

Figure 1. Simulated scatter at the nadir view for total column PW versus 2616–960 cm^{-1} dBT over an ocean surface with a wind speed of 10 m s^{-1}, following *Wu and Smith* [1997]. Simulations (a) without IR channel noise and (b) with channel noise, a function of channel and scene BT. The gray contours indicate the thresholds between cloudy and uncertain sky. The dashed black line is the threshold function developed by *Hutchison et al.* [1995].

and 903 (960.664 and 961.060 cm^{-1}, abbreviated to "960" cm^{-1}), and channel 2333 (2616.383 cm^{-1}, abbreviated to "2616" cm^{-1}); the channel numbering is based on the full set of 2378 channels. The dBT is defined as 2616–960 cm^{-1}. Channels 902 and 903 are located just to the side of the 9.6 μm O_3 fundamental, and in between some weak H_2O and CO_2 absorption lines, in a spectral region of relatively high transmittance. Channel 2333 is the cleanest window channel in the entire AIRS spectrum [*Aumann et al.*, 2004]; it is located in between a few CH_4 and H_2O absorption lines, and has a much smaller H_2O vapor continuum contribution than the 960 cm^{-1} region.

[10] In this section, we describe the general approach to cloud detection using total column PW estimates to define the range of cloudy sky dBT between multiple channels in the IR spectrum. Clear-sky simulations are used to develop thresholds between combinations of dBT and PW values to ascertain whether a given measurement contains cloud or not. Generally speaking, cirrus tend to have dBT > 0; on the other hand, uniform stratus fields that exist over the subtropical oceanic upwelling regions often have dBT < 0 [*Lee et al.*, 1997]. However, observations of shallow cumulus, deep convection, midlevel clouds, cirrus overlying lower water cloud, and even some very thin cirrus sometimes have dBT identical to clear-sky observations of dBT. Thus this method is best used as complimentary to existing methods. Its strength lies in the detection of thin cirrus at nighttime, which will be the focal point of this work. Clear-sky simulations are used to define the boundaries between "cloudy" and "uncertain" sky conditions; the uncertain category contains the clear footprints and some of the cloudy footprints. This results from the fact that some cloud types can have the same dBT as clear sky.

[11] To define the clear-sky range of dBT = dBT(PW), we simulate the dBT between 2616 and 960 cm^{-1} using the AIRS radiative transfer algorithm (AIRS-RTA), a computationally efficient model designed for the AIRS physical retrievals [*Strow et al.*, 2003]. Top-of-atmosphere (TOA) clear-sky radiances are simulated using 8350 soundings over the entire course of the year 2003; a total of 13 coastal and island radiosonde sites were chosen that span tropical to polar latitudes in both hemispheres. For a fixed column value of PW, the temperature and humidity profiles vary with spatial location and time. To apply this technique over as wide a spatial region as possible, soundings were chosen that span a large geographical and temporal space in order to reduce the biases that result from site-specific tendencies in dBT. Soundings were manually inspected for spurious values of temperature and humidity; corrupted sounding data can lead to significant errors in the simulated dBT.

[12] The results of the simulations for the nadir view angle are presented in Figure 1. Figure 1a (Figure 1b) presents simulations without (with) the inclusion of channel and BT-dependent noise equivalent delta temperature (NEdT). Each point represents the simulation of dBT for clear sky using one radiosonde observation. There are three general features to note for the simulations without channel noise: (1) dBT increases nonlinearly with PW unlike the clear/cloudy threshold developed by *Hutchison et al.* [1995], (2) there is a somewhat well-contained range of scatter in dBT for clear sky, and (3) the degree of scatter in dBT increases with PW.

[13] In Figure 1a, the width of scatter in dBT at a fixed PW is strictly the result of temperature and humidity profile variability in the radiosondes. In Figure 1b, notice the width of scatter in dBT increases considerably for the lowest values of PW due to the inclusion of channel noise. Channel noise increases with colder scene BT; thus, in the drier (and colder) geographical locations (e.g., polar latitudes), the channel noise becomes more important in defining the envelope of scatter than in the more moist (and warmer) locations. The two curves bounding the scatter are the thresholds used in this method to define the difference between cloudy and uncertain sky. The variance (σ^2) in the scatter of dBT is calculated for PW bins in 1 mm increments. These (arbitrary) curves approximately represent the $2 \times \sigma^2$ value either side of the mean of the scatter, plus an additional 5 mm of PW added (subtracted) from the

Table 1. Coefficients for the Sixth-Order Polynomial Fits of the Cloudy/Uncertain Thresholds[a]

θ_a	θ_s	a_0	a_1	a_2	a_3	a_4	a_5
			Uncertain Sky Lower Bound Coefficients				
0	0	8.97E−2	−4.24E−2	4.41E−3	−1.27E−4	2.03E−6	−1.19E−8
13.48	15	9.31E−2	−4.31E−2	4.51E−3	−1.31E−4	2.11E−6	−1.24E−8
22.37	25	1.01E−1	−4.42E−2	4.71E−3	−1.39E−4	2.26E−6	−1.34E−8
26.76	30	1.09E−1	−4.47E−2	4.84E−3	−1.45E−4	2.38E−6	−1.41E−8
31.09	35	1.23E−1	−4.52E−2	4.99E−3	−1.53E−4	2.54E−6	−1.51E−8
35.36	40	1.47E−1	−4.53E−2	5.16E−3	−1.62E−4	2.74E−6	−1.65E−8
39.54	45	1.87E−1	−4.45E−2	5.31E−3	−1.74E−4	3.00E−6	−1.82E−8
43.61	50	2.53E−1	−4.20E−2	5.41E−3	−1.88E−4	3.35E−6	−2.06E−8
47.52	55	3.63E−1	−3.65E−2	5.39E−3	−2.05E−4	3.82E−6	−2.39E−8
			Uncertain Sky Upper Bound Coefficients				
0	0	−1.54E−2	1.71E−2	3.73E−3	−9.50E−5	1.33E−6	−7.66E−9
13.48	15	−1.20E−2	1.79E−2	3.87E−3	−9.87E−5	1.37E−6	−7.84E−9
22.37	25	−3.58E−3	1.93E−2	4.14E−3	−1.06E−4	1.45E−6	−8.17E−9
26.76	30	6.42E−3	2.04E−2	4.33E−3	−1.10E−4	1.50E−6	−8.37E−9
31.09	35	2.42E−2	2.19E−2	4.56E−3	−1.16E−4	1.55E−6	−8.55E−9
35.36	40	5.54E−2	2.39E−2	4.82E−3	−1.22E−4	1.60E−6	−8.64E−9
39.54	45	1.09E−1	2.66E−2	5.10E−3	−1.28E−4	1.63E−6	−8.53E−9
43.61	50	2.01E−1	3.02E−2	5.38E−3	−1.32E−4	1.59E−6	−7.98E−9
47.52	55	3.54E−1	3.51E−2	5.58E−3	−1.30E−4	1.44E−6	−6.54E−9

[a]The lower (upper) bound indicates the lower (higher) value of dBT for the uncertain sky designation. The lower (upper) bound appears as the threshold on the left (right) in Figure 1. If the AIRS dBT falls outside of the two bounds, "cloud" is detected. The instrument scan angle (θ_a) and surface emission angle (θ_s) are listed for reference. A linear interpolation of the threshold between the different scan angles is suggested and used in this work. The optimal range the thresholds are designed for is 10 < PW (mm) < 65; regions of PW outside of this range should be treated with caution. The form of the best fit equation is $BT_{bdry} = a_0 + \sum_{n=1}^{5} a_n x^n$, where x is the total column PW in mm and BT_{bdry} is the lower or upper boundary of the uncertain sky. Read 8.97E−2 as 8.97×10^{-2}.

$2 \times \sigma^2$ value, to yield the left-hand (right-hand) curves shown in Figure 1. A sixth-order polynomial was used for the curve fitting; the coefficients for the best fit are listed in Table 1. The fitted curves are valid for 10 < PW (mm) < 65, and should be used with caution outside of this range. Application of this dynamic threshold technique to AIRS/AMSU data sets is computationally very efficient; about 5 seconds are needed to process an entire AIRS granule on a Macintosh Powerbook G4.

[14] In order to determine the "width" of the uncertain sky boundaries in terms of cirrus τ_{IR} (extinction optical depth at 10.4 μm), a series of simulations were performed where τ_{IR} was varied in a standard tropical atmosphere discussed above. Because of the difficulty in retrieving accurate and verifiable profiles of temperature and humidity on a global basis, it is necessary to consider the fundamental vertical variability of these profiles, which cause a certain degree of scatter in dBT = dBT(PW), as shown in Figures 1a and 1b. Thus we must understand the range of dBT in terms of τ_{IR} in the uncertain range to determine the sensitivity of this technique to the optically thinnest cirrus.

[15] In Figure 2, the dBT difference between that of a cloudy and clear sky is related to τ_{IR} as a function of ice scattering model. All simulated cirrus dBT values shown in Figure 2 use the Standard Tropical atmospheric profile as input, and a single layer of cirrus is simulated from 11 to 12 km. To investigate the ice habit effect on the simulation, we used the following shapes: spheres, cylindrical aggregates, and hexagonal cylinders, as a first approximation. As discussed below, the single-scattering properties for these shapes are readily available for direct radiative transfer calculations. The approximate width of the cloudy sky thresholds in dBT space (from Figure 1) for the Standard U.S. (column PW ≈ 20 mm; dBT ≈ 0.9 K) and Tropical (column PW = 40 mm; dBT = 1.8 K) atmospheres are marked with the horizontal gray bars. These gray bars highlight the approximate range in τ_{IR} for the estimated "worst-case scenario" minimum detection threshold of cirrus. This does not correspond to the lowest detectable τ_{IR} for any given cirrus cloud, but it is the estimate of τ_{IR} above which nearly all cirrus is detected.

[16] The worst-case scenario of τ_{IR} for detected thin cirrus is on the order of 0.1–0.15 in the Standard Tropical atmosphere, and is around 0.05–0.1 in the Standard U.S. atmosphere; the small range of values are a result of the different modeled particle habits and sizes. Cirrus with much lower τ_{IR} can be detected than Figure 2 implies, but not all cirrus with τ_{IR} less than the values given will be detected. The temperature and humidity profiles determine to a large degree the "detectability" of a given cirrus cloud. Also, there is a strong sensitivity to the assumed cloud height that is employed in the model. As a rule of thumb, the τ_{IR} thresholds increase (decrease) for lower (higher) cirrus altitudes. For cirrus at 8–9 km, the τ_{IR} thresholds are approximately 1.5 times greater than those for cirrus at 11–12 km (not shown). Caveats to the minimum τ_{IR} threshold are elaborated on in section 4.

[17] We have used the single-scattering properties for spheres, cylindrical aggregates, and hexagonal cylinders in the 10 μm window readily available from *Mishchenko and Travis* [1998], *Baran* [2003], and *Baran et al.* [2002], respectively, in conjunction with simulations of the radiative properties of cirrus by the Code for High-resolution Accelerated Radiative Transfer with Scattering (CHARTS) [*Moncet and Clough*, 1997]. As discussed by *Baran* [2003] and *Baran et al.* [2002], some of their results have been verified with the single-scattering properties of ice particles computed from the combination of a modified geometric

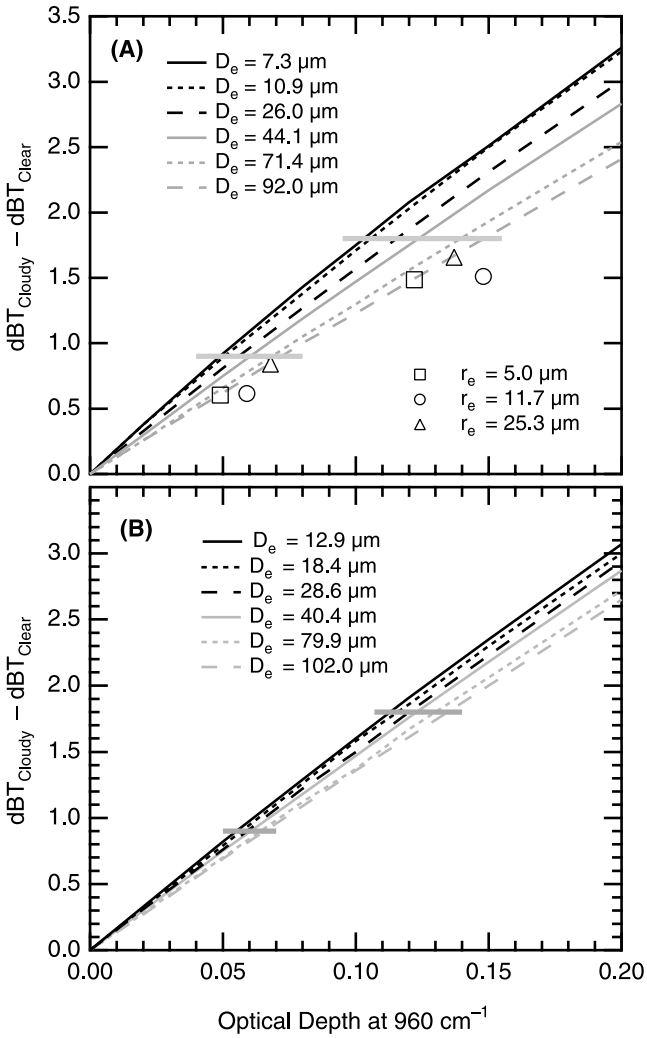

Figure 2. (a) IR optical depth versus cloudy–clear-sky $dBT_{2616-960}$ for cylindrical aggregates [*Baran*, 2003] and spheres [*Mishchenko and Travis*, 1998]. (b) As in Figure 2a except for hexagonal cylinders [*Baran et al.*, 2002]. All clear-sky and cloudy sky simulations were calculated using a Standard Tropical atmosphere. In the cloudy simulations, a cloud height of 11–12 km was used. For the U.S. Standard atmosphere, the results are nearly identical and thus are not shown. The gray lines represent the approximate dBT value in between the two thresholds shown in Figure 1, for the Standard Tropical (dBT = 1.8 K) and Standard U.S. (0.9 K) atmospheres.

optics approach and the finite difference time domain method developed by *Yang and Liou* [1996] and *Yang et al.* [2000]. For the spherical ice particles, we assumed a power law size distribution with an effective variance of 0.25. The r_e is defined as the ratio of the integrated volume over the particle size distribution to the integrated geometric cross-sectional area over the same distribution [*Mishchenko and Travis*, 1998]. The effective diameter (D_e) of the cylindrical aggregates and hexagonal cylinders are similarly defined [*Baran et al.*, 2002; *Baran*, 2003]. Details of the microphysical characteristics of cirrus leads to a considerable effect on simulated radiances; this has been demonstrated by *Liou et al.* [2000] and *Rolland et al.* [2001] and more recently by *Baran* [2004], *Huang et al.* [2004], *Rädel et al.* [2003], and *Wei et al.* [2004]. Thus the simulations presented herein are complementary to these efforts and should be viewed as approximate, and not representative of all cirrus types and atmospheric configurations.

[18] Some important assumptions were made for the simulated clear-sky radiances. First, the skin temperature (T_s) is set equal to the temperature at the lowest atmospheric level in the sounding (T_a). This assumption is most valid over the tropical and subtropical oceans, and breaks down over the higher latitude oceans, especially downwind of continents in the winter hemisphere, where advection of cold continental air over the ocean leads to $T_{s-a} \gg 0$. When T_{s-a} exceeds a few kelvins, the dBT is significantly affected. Figure 3 shows the same simulations as in Figure 1a, except T_{s-a} is set to +10, +5, −5, and −10. Notice that the departures of T_{s-a} have the least (greatest) sensitivity reflected in dBT for the dry (moist) soundings. Thus there are two competing influences for T_{s-a} departures from zero: the sensitivity is greatest (least) in the moist (dry) atmospheres, but the largest departures tend to occur where the atmosphere is drier and colder, with $T_{s-a} \gg 0$.

[19] Second, we assume the surface emissivity follows for an oceanic surface with a wind speed of 10 m s^{-1} after *Wu and Smith* [1997]; scan angle effects are included in the simulations (not shown). Initially, application of this method is limited to oceanic surfaces where these assumptions usually hold. However, this technique is only limited by the potential accuracy of T_{s-a} and surface emissivity retrievals; emissivity is highly variable over land, especially over barren mineral surfaces, which can greatly impact the spectral dependence in radiance for a clear-sky simulation [*Fishbein et al.*, 2003]. Figure 4 shows the same clear-sky simulations presented in Figure 1a, except the surface emissivity is representative of conifer and deciduous forest, tundra, and quartz. In Figure 4, note that the quartz and deciduous forest surfaces lead to substantially different results compared to a typical oceanic surface, as shown in Figure 1 but that conifer forest and tundra are not very different from typical oceanic surfaces. The thresholds obtained from Figure 1a are superimposed on Figure 4 to show the degree to which the scatter remains within the thresholds when changing surface type. Improvements in retrievals of T_{s-a} and surface emissivity from spaceborne measurements will inevitably lead to a greater geographical applicability of this method.

3. Observations

3.1. AIRS/AMSU Suite

[20] Each day over 2.9 million IR spectra are taken by AIRS, with 9 AIRS footprints colocated within a single AMSU-A footprint. Both AIRS and AMSU-A measurements are used synergistically to retrieve the myriad of atmospheric and surface products, including temperature and humidity profiles [*Susskind et al.*, 2003]; these retrievals are performed over the scale of the AMSU-A footprint, yielding 324,000 retrievals per day. Validation of the retrieved products is ongoing [*Fetzer et al.*, 2003, 2004; *Gettelman et al.*, 2004].

[21] Figure 5a presents a typical granule within the tropics; a potpourri of cloud activity abounds, including

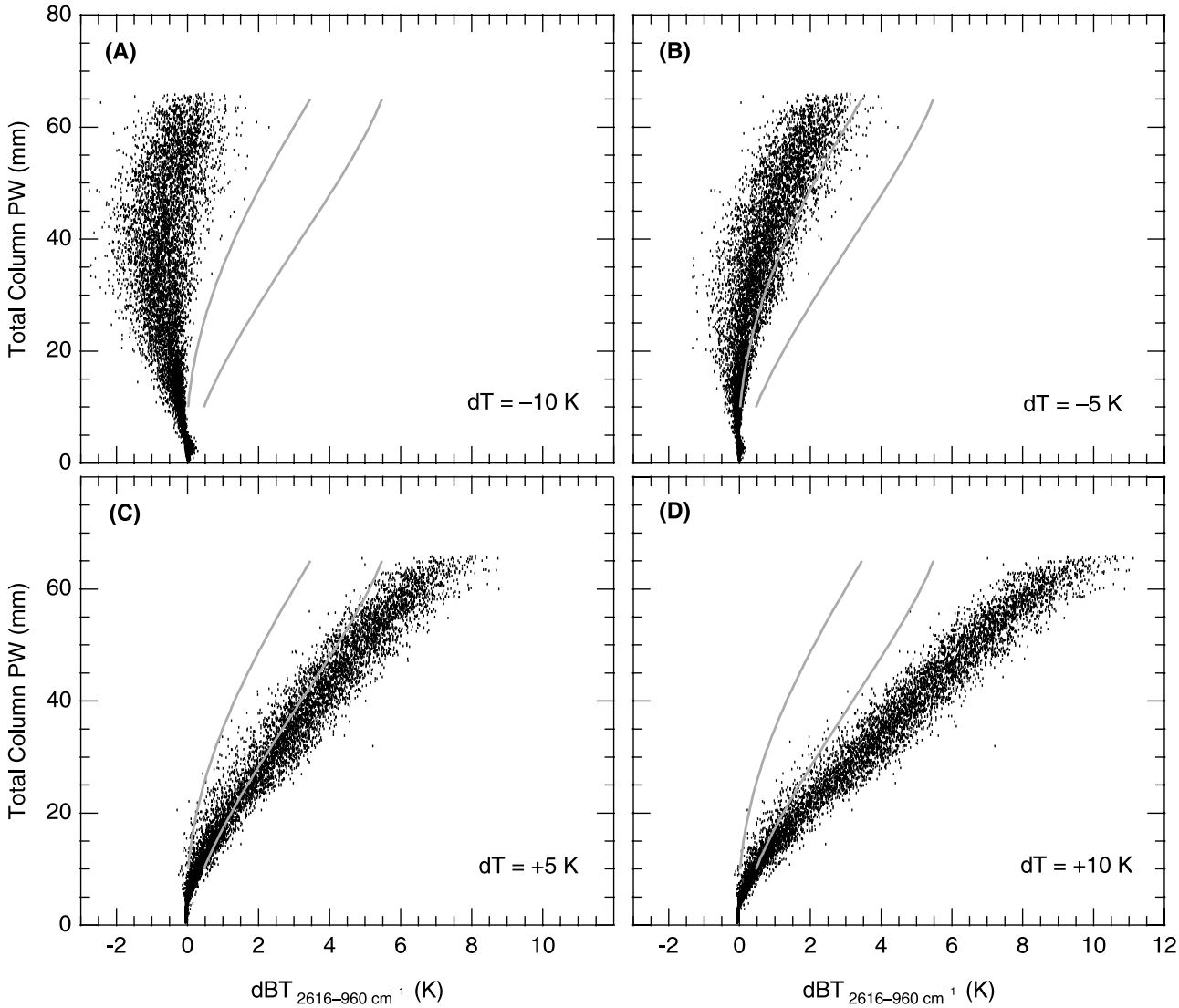

Figure 3. Simulated scatter diagrams with adjusted $\Delta T = T_{skin} - T_{air} \neq 0$. Thresholds between cloudy and uncertain sky cover from Figure 1 are superimposed. All other physical quantities used in the simulations are as described for Figure 1a; no IR channel noise is included in these simulations.

deep convection, cirrus, altocumulus and altostratus, as well as stratus and scattered cumulus clouds, which often occur simultaneously in multiple layers within a single footprint [*Baum et al.*, 2003]. This is based on studying the ARM cloud boundaries for numerous coincident AIRS footprints, to be discussed in section 3.2. Figure 5b shows the total column PW for the same scene. Despite the expected high amounts of PW over the entire region, a significant amount of variability exists, with higher levels of PW coinciding with the more extensive cloud masses. Figure 5c shows dBT; comparisons with split window differences limited to the mid IR windows (not shown) indicates a much greater sensitivity of cirrus using SW − LW differences, as indicated by *Lutz et al.* [2003].

[22] After applying the cloud detection method discussed in section 2, the cloud detection "map" is presented in Figure 5d. The color scale is the same as Figure 5c, except regions of uncertain sky are denoted as white and cloudy regions remain colored. The circled regions indicate particular clouds of interest. In the upper right in and around an area of deep convection, the speckled pattern over the convective towers is a result of the cold BT values. NEdT values at 2616 cm^{-1} increase substantially for BT < 215 K, but much less so for 960 cm^{-1}; thus the speckled pattern is a result of the high level of noise at 2616 cm^{-1}. Just to the right, notice the region of dBT > 20 K; this is a common feature seen in anvil regions surrounding areas of cumulonimbus, in the tropics and elsewhere, because of the preponderance of small ice particles [*Kahn et al.*, 2003].

[23] The highlighted region in the middle left of the granule around an area of midlevel cloudiness indicates a "ring" of uncertain sky surrounding the midlevel clouds. There is a transition of cloud that is detected outside of the right boundary in Figure 1, to cloud detected outside of the left boundary. This feature is seen on occasion, and may imply a transition in cloud microphysics; the spectral features of mixed phase cloud can change significantly from water or ice cloud alone [*Yang et al.*, 2003], even

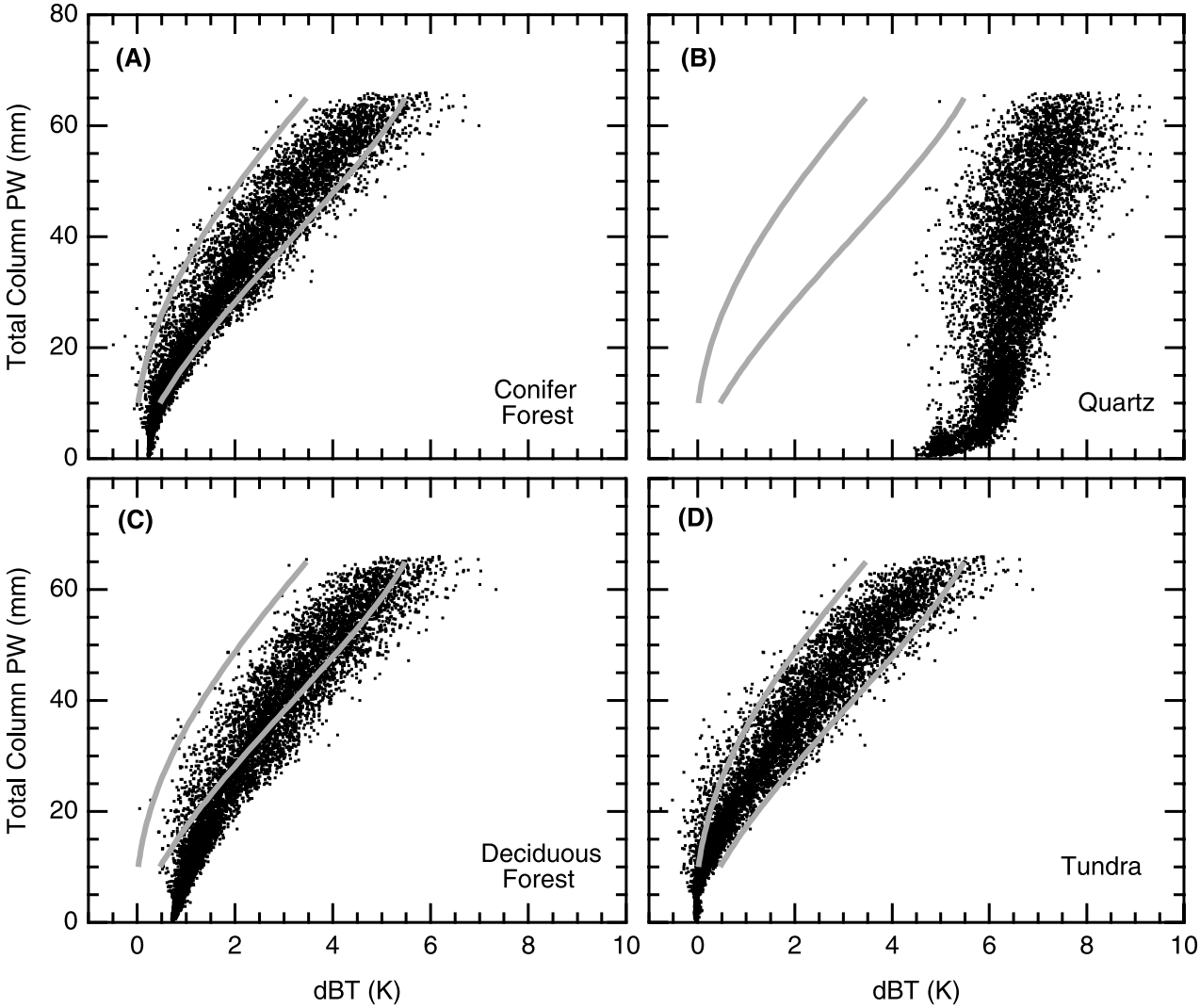

Figure 4. Simulated nadir view of dBT for four different land types. Cloud detection thresholds (for an ocean surface) from Figure 1 superimposed for comparison purposes. (a) Conifer forest with emissivity of 0.9897 and 0.9889 at 960 and 2616 cm^{-1}, respectively, (b) quartz (0.860 and 0.925), (c) deciduous forest (0.976 and 0.983), and (d) tundra (0.989 and 0.969). Emissivity values are taken from land types presented by *Fishbein et al.* [2003].

over the horizontal scale of meters [*Chylek and Borel*, 2004]. Another possibility is cirrus overlying lower-level water cloud [*Nasiri and Baum*, 2004]. In the lower right, another area of cloud is detected outside of the left boundary in Figure 1. The area of cloudiness appears to be low-level, stratiform cloudiness (judging from the very high BT_{960}), much like the coastal stratus near oceanic upwelling regions on the west side of the subtropical continents [e.g., *Lee et al.*, 1997]. Inspection of granules in these geographical regions confirms that low-level stratiform regions can produce significant negative values of dBT (not shown).

[24] Similar maps as shown in Figure 5 have been manually inspected for hundreds of AIRS granules spanning all latitudes, seasons, and surface types. The limitations imposed by our assumptions for T_{s-a} and surface emissivity hinder the applicability of this method over land and for high latitude oceans; manual inspection of cloud detection maps for these geographical regions show this to be the case. To validate the results of the cloud detection procedure in a typical tropical setting, we use some of the ground-based measurements of clouds conducted at the ARM Tropical Western Pacific (TWP) site located at Manus Island (2°S 147.5°E). The instrumentation lies just to the east of Manus Island on a small adjacent island only a few kilometers in width; the main body of Manus Island is approximately 90 km long in the W-E direction and 30 km wide in the N-S direction, large enough to fill several AIRS footprints completely with land. On a number of occasions the approximate shape of Manus Island is noted in the AIRS thermal IR imagery. Since the ARM site is located just to the east of the main body of Manus Island, it is expected that T_{s-a} and surface emissivity effects on dBT will be minimal in most cases.

3.2. Manus Island ARM Site

[25] There are numerous passive and active remote sensing instruments at the ARM TWP sites that are sensitive to cloudiness. To validate the new method of cloud detection,

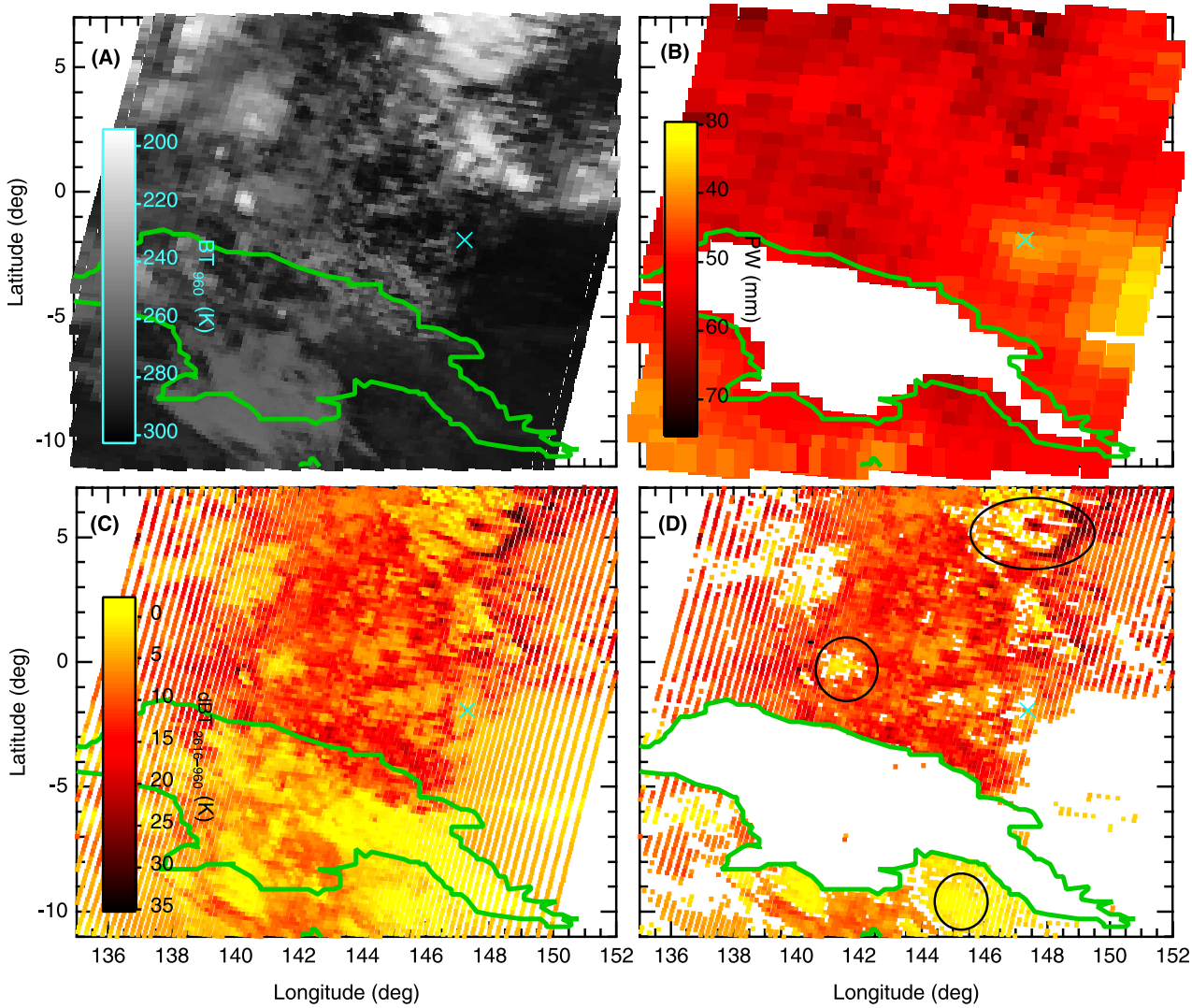

Figure 5. Case study for the nighttime AIRS granule taken on 20 June 2003. The blue cross denotes the location of the ARM instrument site on Manus Island. (a) BT_{960}, (b) total column PW in mm, (c) SW − LW (2616–960 cm^{-1}) BT difference, and (d) cloud detection map. For Figure 5d, all of the colored pixels are as in Figure 5c, where the white areas indicate regions of uncertain sky as determined by the combined AIRS/AMSU method. The footprint size in Figures 5c and 5d is reduced to highlight the areas of uncertain sky cover surrounding particular cloud masses.

we use the value-added product that combines the capabilities of several active sensors: a laser ceilometer, a micropulse lidar, and a millimeter wave cloud radar [*Clothiaux et al.*, 2000]. Each instrument has particular capabilities and limitations that are related in part to cloud height, cloud optical depth, and hydrometeor size, among others. The instruments are combined in a synergistic fashion for a comprehensive cloud boundary detection tool; see *Clothiaux et al.* [2000, and references therein] for further details.

[26] A total of 89 AIRS granules that coincide with Manus Island in which the ARM value-added product is available are used to validate the cloud detection method. These cases span a very large range of sky conditions: clear, partly overcast, overcast, and precipitating skies. The observed clouds range from fair weather cumulus to deep convection, and from optically thin to thick cirrus, among others. We present results for all 89 of the coincident measurements, and inspect every case to understand why the techniques compare favorably or not.

[27] A cloud, as defined by the technique presented in the Methodology, is a combination of PW and dBT that falls outside of the uncertain sky boundaries as in Figure 1. As discussed previously, some clouds may fall within the uncertain sky boundaries, especially low cumuliform clouds, those near cold convective cores, some midlevel clouds, cirrus overlying water cloud, and even some very optically thin cirrus. The strength of this technique lies in the detection of cirrus above $\tau_{IR} > 0.1$, although it can be problematic to discern cirrus from other cloud types by this technique alone.

[28] A cloud, as defined by the value-added product [*Clothiaux et al.*, 2000], is simply an observation that contains at least one cloud top and base. Comparing a

Table 2. Comparison of Manus Island ARM Site Value-Added Product and the Proposed Cloud Detection Technique[a]

	ARM Cloud 1[b]	ARM Cloud 2[c]	ARM Clear
AIRS cloud	52 (59)	52 (57)	6 (3)
AIRS uncertain	21 (23)	6 (10)	10 (4)

[a]See *Clothiaux et al.* [2000] for the value-added product. The first value of each entry indicates the total number of cases in which the two techniques "agree" or "disagree" if the ARM cloud observation is defined as the 6 min window beginning and ending with the time of the coincident AIRS granule. The value in parentheses is defined as the 6 min window ±24 min, for a total of 54 min; any cloud within this time period makes the ARM measurement "cloudy." Comparison of ARM Cloud 2 and ARM clear shows that the AIRS and ARM detection techniques agree 84% (82%) of the time for the 6 min (54 min) window.

[b]Inclusion of all 89 coincidences of ARM measurements and AIRS overpasses.

[c]Same as ARM cloud 1, except the 15 ARM site observations for shallow cumulus only are removed. AIRS dBT is relatively insensitive to shallow, tropical cumulus; thus the ARM Cloud 2 and ARM clear values more appropriate sets of observations for comparison.

measurement from a satellite platform that spans a horizontal scale of 13.5–20 km with a point measurement from the surface is a difficult task; individual cloud elements do not simply advect around with the mean wind. They are constantly evolving (generating or dissipating) over the timescale of minutes or less. To make the comparison between AIRS and the ARM site, we use two methods of defining when cloud has been detected by the ARM site: if cloud boundaries are detected anytime within the 6 min period defined by the beginning and end time of the coincident AIRS granule, or if cloud boundaries are detected anytime within ±24 min either side of the granule, for a total of 54 min. Inevitably, there is some sensitivity to this choice, and this will be discussed further as the results are presented. Thus the ARM site indicates whether the sky is either clear or cloudy; this proposed method indicates whether the sky is of uncertain cover or cloudy.

[29] Comparison of detected clouds by both methods is summarized in Table 2. Upon first view of the results, one sees that AIRS and ARM agree in 82–84% of the cases when shallow cumulus cases are not considered, with the percentage depending on the time window definition of an ARM cloudy observation. Manus Island is characterized by frequently cloudy skies; clouds are observed 82% of the time over the 6 min window, which increases to 92% over the 54 min window, implying very few AIRS footprints are completely clear near Manus Island at nighttime.

[30] In Figure 6 each case is partitioned into a cloud category, in order to understand more about why particular cases agree or disagree. Upon further inspection of the cases in which there is disagreement ("ARM cloudy/AIRS uncertain" or "ARM clear/AIRS cloudy"), a majority of the cases disagree because ARM detects shallow cumulus clouds in which AIRS dBT is insensitive. Two cases disagree because the cold BTs over convection produce substantial noise at the 2616 cm^{-1} channel, allowing the dBT to fall within the uncertain category. A few other cases are in disagreement in regions of midlevel cloudiness, possibly consistent with spectral signatures of mixed phase [*Yang et al.*, 2003] or multilayer [*Nasiri and Baum*, 2004]

	ARM Cloud[1]		ARM Clear	
AIRS Cloud	9 (*7*)	9 (*11*)	–	–
	17 (*18*)	17 (*21*)	–	–
	0 (*2*)	–	–	6 (*3*)
AIRS Uncertain	–	–	–	–
	4 (*8*)	2 (*2*)	–	–
	15 (*13*)	–	–	10 (*4*)

[1] Representative of 1st column in Table 2.

Figure 6. Comparison of Manus Island ARM value-added product [*Clothiaux et al.*, 2000] and the proposed cloud detection technique, with cloud types broken into categories. Summation of all cases equals the totals presented in Table 2. Each of the four possible AIRS and ARM site combinations are broken into six subcategories: (1) uniform single or multilayered cirrus (top left), (2) uniform single or multilayered cirrus with underlying midlevel clouds (top right), (3) patchy single or multilayered cirrus alone, or with midlevel clouds (middle left), (4) deep, precipitating cumulus or cumulonimbus (middle right), (5) shallow cumulus with tops less than 5 km (bottom left), and (6) clear skies (bottom right). All cloud categories are defined by the ARM site sky observations. Clouds are identified as "cirrus" if cloud bases are 10 km or higher, "midlevel" clouds have bases and tops located between 5 and 10 km, and shallow cumulus clouds have tops below 5 km. The 5 and 10 km levels roughly correspond to the 0°C and −40°C levels in a tropical atmosphere, which can be expected to be the approximate bounds of liquid water, mixed liquid and ice, and ice only clouds. In categories 1–4, we allow observations of low-level cumulus clouds to coexist, as they have a minimal impact on dBT.

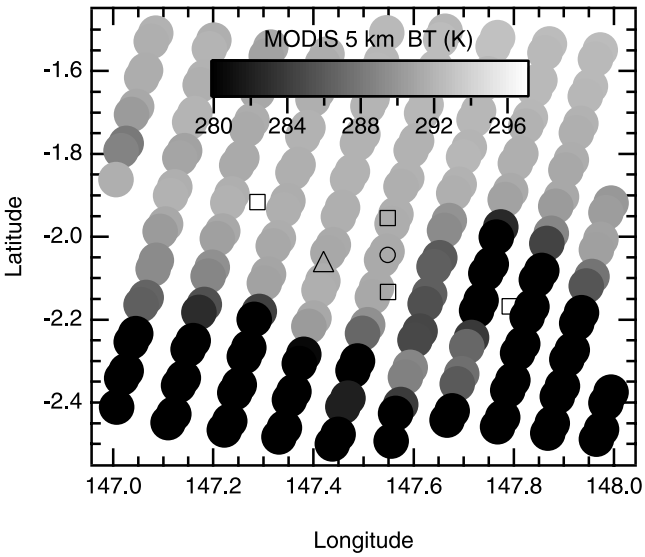

Figure 7. The 2 May 2003 1506 UTC granule to compare AIRS subfootprint-scale BT variability using MODIS 5 km pixels (solid gray scale circles). The center of the AIRS footprint is noted with the small open circle in the center. The squares are the four corner latitude/longitude pairs that mark the approximate location of the AIRS footprint. The ARM Manus Island site is indicated with the triangle; note that its location is on the edge of the AIRS footprint. At high scan angles, AIRS footprints become more elongated [*Aumann et al.*, 2003].

cloudiness. The ARM site is located just outside of the AIRS footprint for a couple of cases, and in a few others the AIRS footprint is located such that a portion of it is positioned over the main body of Manus Island to the west of the ARM site, especially for the elongated footprints at a high scan angle. Because a significant portion of the footprint is located over land, this could somewhat violate the assumptions about T_{s-a} and surface emissivity for the Manus Island ARM site. The impact on dBT may be enough to shift the footprint from the uncertain category to the "cloudy" category, or vice versa, in a borderline case.

[31] A majority of the remaining cases in disagreement appears to be related to the discrepancy between the scale of the AIRS footprint and the very small field of view of the ARM site measurements. A small patch of cloud over the ARM site might be surrounded by clear sky, or the ARM site may observe a small patch of clear sky within a widespread cloud field. Areas of optically thin and thick cloud may produce a similar effect. For the cases in disagreement, we have inspected radiances and BTs in the atmospheric window using MODIS channels to investigate the AIRS subfootprint variability at the 1 and 5 km scales. The smaller spatial scale variability of BT (at 5 km) allows us to explain several of the cases that disagree; if the ARM site observes cloudy (clear) skies and AIRS observes uncertain (cloudy) skies, the MODIS pixel closest to the ARM site has a lower (higher) BT than those averaged over the AIRS footprint. Other potential reasons for disagreement should be explored in the future, including geolocation errors of AIRS footprints [*Gregorich and Aumann*, 2003].

[32] Figure 7 shows a case in which the two cloud detection methods disagree, and the disagreement is consistent with AIRS subfootprint-scale cloud variability; the ARM site indicates clear sky, and the proposed cloud detection method indicates cloud. The MODIS BT pixel size shown is 5 km, and represents the nighttime overpass on 5 May 2003. MODIS 1 km radiances for channel 31 were also investigated, indicating a very similar result. Notice the elongated nature of the AIRS footprint; at high scan angles it is far from circular in shape, and is on the order of 20 km in length. The ARM Manus Island site is located at the edge of the AIRS footprint. The closest MODIS pixel to the ARM site is 291.8 K; in contrast, the average MODIS BT over the entire AIRS footprint is 287.8 K. The coldest MODIS pixel within the AIRS footprint is 270.7 K, while the warmest is 292.3 K. In this case, the ARM site was free of cloud cover at the time of the AIRS measurement, so this implies the AIRS footprint contained enough cloud cover to allow dBT to exceed the uncertain sky boundaries.

4. Discussion

[33] The thresholds which define cloudy and uncertain sky cover developed in the Methodology and presented in Table 1 are somewhat arbitrary and are based on some assumptions that do not hold globally; T_{s-a} is assumed to be zero, and surface emissivity is representative of an oceanic surface with wind speeds of 10 m s^{-1}. The vertical variability in temperature and humidity leads to a substantial variability in dBT, increasing with larger PW amounts. The PW values used are those from the combined AIRS/AMSU retrievals [*Susskind et al.*, 2003], and are representative of AMSU-A fields of view, about 45 km at nadir view. Subfootprint AMSU-A variability in PW values can be significant enough to impact some borderline uncertain and cloudy sky decisions, which is especially true for the most tenuous cirrus clouds. Instrument noise in the IR channels leads to an uncertainty in dBT, although it is minimal at high BTs; over cold scenes, such as those in polar latitudes or over deep convection, noise plays a much bigger role.

[34] When making intercomparisons of cloud observations between the ARM site and the AIRS footprint scale (~15 km), numerous challenges present themselves. If the cloud is not homogeneous over the entire AIRS footprint, the ARM measurement may observe different cloud properties than those averaged over the AIRS pixel. The ARM site observation might be within the AIRS footprint, or just outside of it. If a time series of ARM observations is used along with a mean wind speed to estimate the time necessary to reproduce the horizontal scale of the AIRS footprint, clouds can dissipate and generate on the scale of minutes or less, further complicating the picture. Also, there could be vertical wind shear, with different layers of clouds moving at different wind speeds and directions, complicating the picture even more. The ARM observation may be on the edge of a cloud, while the AIRS footprint may be partially located over a clear scene. As shown in section 3, this can lead to a discrepancy between cloud detection techniques, specifically, one that is surface based, and the other satellite based.

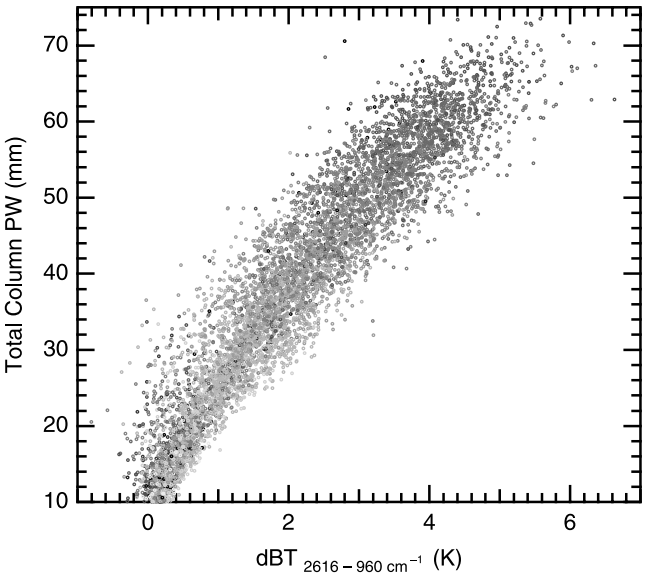

Figure 8. Scatter diagram of simulated dBT as in Figure 1. The gray scale indicates the pressure level where approximately 50% of the total column PW is located above and below it, ranging from 700 mbar (dark gray) to 950 mbar (light gray).

[35] Despite these numerous difficulties, it has been shown that using total column PW measurements to constrain dBT signatures for the purpose of identifying cloud, specifically optically thin cirrus, is encouraging, especially in the tropical oceanic regions where thin cirrus plays an important role in regulating Earth's radiative balance [*Prabhakara et al.*, 1993].

[36] A more accurate retrieval of several physical quantities will lead to a lower τ_{IR} detectability limit, or a more wide-ranging global applicability of this method. These include retrievals of T_{s-a}, as well as surface emissivity, which strongly depends on surface type. Both of these quantities are much more highly variable over land when compared to oceanic surfaces. Retrievals of total column PW at the scale of the AIRS footprint capture the small-scale PW variability more accurately. However, the increased accuracy in retrieved temperature and humidity profiles will inevitably lead toward reducing the range of uncertain sky dBT, as these quantities work in synergy to produce the scatter in dBT shown in Figure 1. The humidity profiles alone likely will not lead to a reduction in the τ_{IR} detectability limit. Figure 8 shows a scatter diagram of PW versus dBT, as in Figure 1, except the overlying gray scale is an indication of the vertical distribution of PW. The gray scale indicates the approximate altitude of the PW vertical distribution where 50% of the PW is located above and below. Unfortunately, this altitude appears to be a function of the PW value, and not dBT.

[37] This suggests that a reduction in the τ_{IR} detectability limit needs to be attempted using improved soundings of temperature and humidity simultaneously, instead of humidity alone. Using the AIRS-RTA in synergy with the retrieved AIRS temperature and humidity profiles may help to reduce the uncertainty of the clear-sky dBT and, hence, to reduce the width of the uncertain sky dBT thresholds. This will require a thorough comparison of retrieved AIRS temperature and humidity profiles with those from radiosondes in both clear and cloudy scenes; this subject is a topic of ongoing work [*Fetzer et al.*, 2003, 2004; *Gettelman et al.*, 2004].

5. Conclusions

[38] A computationally efficient method of cloud detection is presented that combines the total column precipitable water (PW) with radiances in the IR window channels, using the colocated measurements of the Advance Microwave Sounding Unit A (AMSU-A) and the Atmospheric Infrared Sounder (AIRS), residing on EOS-Aqua. The basic principle involves the constraint imposed by the effect of the water vapor column on the BT difference between 3.8 and 10.4 μm (2616–960 cm^{-1}) (dBT). The range of dBT for "clear" sky is produced by simulating radiances with the AIRS radiative transfer algorithm (AIRS-RTA) [*Strow et al.*, 2003]. Clouds are detected when the observed dBT falls outside of the defined dBT threshold. The clear-sky simulations are interpreted as uncertain sky cover for the purposes of cloud detection as many clouds have identical dBT as clear-sky dBT.

[39] A total of 8350 soundings launched around the globe near ocean basins and from islands are used to initialize the atmospheric temperature and humidity profiles in the AIRS-RTA. Because of the natural variability in temperature and humidity profiles, the dBT for a particular value of PW is not a constant value. Instrument noise in the IR channels is considered in the simulated dBT, in addition to the scan angle dependence in dBT. Surface emissivity for an oceanic surface with a wind speed of 10 m s^{-1} is assumed for all simulations, and the impact of variable land surfaces on the results was shown to be significant; the thresholds presented in this work will not generally be applicable over land. Lastly, the skin temperature (T_s) and air temperature at the lowest atmospheric level (T_a) were assumed equal. The combination of these assumptions prevent a global applicability of this cloud detection method; however, better estimates of T_{s-a} and surface emissivity will inevitably lead to an applicability over a larger geographical range. Current limitations make this method most applicable over the tropical and subtropical oceans, and perhaps the midlatitude oceans during the summertime; these are locations where the assumptions generally hold. Highly variable emissivity and $T_{s-a} \neq 0$ at nighttime over land make this method somewhat ineffective, especially for the optically thinnest cirrus.

[40] Comparisons between this method and the ARM value-added product are made [*Clothiaux et al.*, 2000]. Out of a total of 89 coincident measurements over the ARM TWP Manus Island site, both are in agreement for 82–84% of the cases. However, closer inspection of the cases in which there is disagreement shows that a few are due to cold cumulonimbus scenes, which can lead to a dBT that falls within the uncertain sky boundaries. A few cases are associated with midlevel and multilayered cloudiness, which has been shown to have spectral characteristics significantly different from water or ice phase clouds. Most of the other cases are associated with sub-AIRS-scale footprint cloud variability.

[41] Simulated thin cirrus radiances for ice spheres, hexagonal cylinders, and cylindrical aggregates were made in two different atmospheres: the U.S. standard atmosphere, and a standard tropical atmosphere. The worst-case scenario of τ_{IR} for detected thin cirrus is on the order of 0.1–0.15 in the tropical atmosphere, and is near 0.05–0.1 in the drier and cooler standard atmosphere. The τ_{IR} values are representative of the width in the range of dBT for the two respective atmospheres. Some cirrus with much lower τ_{IR} can be detected, but nearly all single-layer cirrus with τ_{IR} greater than the values given will be detected.

[42] As incremental improvements in retrieved values are achieved for some or all of the aforementioned physical quantities, even thinner cirrus will be detected, applicable over an increasingly large geographical region of the globe. Improved cirrus detection will lead to an improved global cloud climatology, which in turn will lead to improvements in climate and numerical weather prediction models through intercomparisons of data and model results, and improvements in model representations of clouds.

[43] **Acknowledgments.** The authors are grateful to George Aumann for many fruitful discussions, to Tony Clough for the use of CHARTS, to Chuck Long for assistance with the ARM value-added product, to Anthony Baran for use of the nonspherical ice scattering models, and to two anonymous reviewers for suggested improvements to the manuscript. B.H.K. was partially funded by NASA-ESS fellowship NGT-5-30372. Value-added product data for Manus Island were obtained from the Atmospheric Radiation Measurement (ARM) Program sponsored by the U.S. Department of Energy, Office of Science, Office of Biological and Environmental Research, Climate Change Research Division. All soundings were supplied by the Department of Atmospheric Science at the University of Wyoming's online archive (http://www-das.uwyo.edu). A portion of this work was performed at the Jet Propulsion Laboratory, California Institute of Technology, Pasadena, California, under contract with NASA.

References

Ackerman, S. A., and K. I. Strabala (1994), Satellite remote sensing of H_2SO_4 aerosol using the 8- to 12-μm window region: Application to Mount Pinatubo, *J. Geophys. Res.*, *99*, 18,639–18,649.

Ackerman, S. A., K. I. Strabala, W. P. Menzel, R. A. Frey, C. C. Moeller, and L. E. Gumley (1998), Discriminating clear sky from clouds with MODIS, *J. Geophys. Res.*, *103*, 32,141–32,157.

Aumann, H. H., et al. (2003), AIRS/AMSU/HSB on the Aqua mission: Design, science objectives, data products, and processing systems, *IEEE Trans. Geosci. Remote Sens.*, *41*, 253–264.

Aumann, H. H., D. Gregorich, and D. Barron (2004), Spectral cloud-filtering of AIRS data: Non-polar ocean, paper presented at SPIE Atmospheric and Environmental Remote Sensing Data Processing and Utilization, Int. Soc. of Opt. Eng., Denver, Colo., 4–6 Aug.

Baran, A. J. (2003), Simulation of infrared scattering by ice aggregates by use of a size-shape distribution of circular ice cylinders, *Appl. Opt.*, *42*, 2811–2818.

Baran, A. J. (2004), On the scattering and absorption properties of cirrus cloud, *J. Quant. Spectrosc. Radiat. Transfer*, *89*, 17–36.

Baran, A. J., and J. S. Foot (1994), New application of the operational sounder HIRS in determining a climatology of sulphuric acid aerosol from the Pinatubo eruption, *J. Geophys. Res.*, *99*, 25,673–25,679.

Baran, A. J., S. J. Brown, J. S. Foot, and D. L. Mitchell (1999), Retrieval of tropical cirrus thermal optical depth, crystal size, and shape using a dual-view instrument at 3.7 and 10.8 μm, *J. Atmos. Sci.*, *56*, 92–110.

Baran, A. J., S. Havemann, and D. Mackowski (2002), A database of hexagonal column optical properties for wavelengths ranging between 0.2 μm and 30 μm produced for ANNEX 7, contract 4b/3/02, report, Dep. for Environ. Food and Rural Affairs, London.

Baum, B. A., R. A. Frey, G. G. Mace, M. K. Harkey, and P. Yang (2003), Nighttime multilayered cloud detection using MODIS and ARM data, *J. Appl. Meteorol.*, *42*, 905–919.

Chylek, P., and C. Borel (2004), Mixed phase cloud water/ice structure from high spatial resolution satellite data, *Geophys. Res. Lett.*, *31*, L14104, doi:10.1029/2004GL020428.

Clothiaux, E. E., T. P. Ackerman, G. G. Mace, K. P. Moran, R. T. Marchand, M. A. Miller, and B. E. Martner (2000), Objective determination of cloud heights and radar reflectivities using a combination of active remote sensors at the ARM CART sites, *J. Appl. Meteorol.*, *39*, 645–665.

Comstock, J. M., T. P. Ackerman, and G. G. Mace (2002), Ground-based lidar and radar remote sensing of tropical cirrus clouds at Nauru Island: Cloud statistics and radiative impacts, *J. Geophys. Res.*, *107*(D23), 4714, doi:10.1029/2002JD002203.

Dessler, A. E., and P. Yang (2003), The distribution of tropical thin cirrus clouds inferred from Terra MODIS data, *J. Clim.*, *16*, 1241–1247.

Fetzer, E., et al. (2003), AIRS/AMSU/HSB validation, *IEEE Trans. Geosci. Remote Sens.*, *41*, 418–431.

Fetzer, E. J., J. Teixeira, E. T. Olsen, and E. F. Fishbein (2004), Satellite remote sounding of atmospheric boundary layer temperature inversions over the subtropical eastern Pacific, *Geophys. Res. Lett.*, *31*, L17102, doi:10.1029/2004GL020174.

Fishbein, E., C. B. Farmer, S. L. Granger, D. T. Gregorich, M. R. Gunson, S. E. Hannon, M. D. Hofstadter, S.-Y. Lee, S. S. Leroy, and L. L. Strow (2003), Formulation and validation of simulated data for the Atmospheric Infrared Sounder (AIRS), *IEEE Trans. Geosci. Remote Sens.*, *41*, 314–329.

Gao, R. S., et al. (2003), Evidence that nitric acid increases relative humidity in low-temperature cirrus clouds, *Science*, *303*, 516–520.

Garrett, T. J., H. Gerber, D. G. Baumgardner, C. H. Twohy, and E. M. Weinstock (2003), Small, highly reflective ice crystals in low-latitude cirrus, *Geophys. Res. Lett.*, *30*(21), 2132, doi:10.1029/2003GL018153.

Gettelman, A., et al. (2004), Validation of Aqua satellite data in the upper troposphere and lower stratosphere with in situ aircraft instruments, *Geophys. Res. Lett.*, *31*, L22107, doi:10.1029/2004GL020730.

Gregorich, D. T., and H. H. Aumann (2003), Verification of AIRS boresight accuracy using coastline detection, *IEEE Trans. Geosci. Remote Sens.*, *41*, 298–302.

Holton, J. R., and A. Gettelman (2001), Horizontal transport and the dehydration of the stratosphere, *Geophys. Res. Lett.*, *28*, 2799–2802.

Huang, H.-L., P. Yang, H. Wei, B. A. Baum, Y. Hu, P. Antonelli, and S. A. Ackerman (2004), Inference of ice cloud properties from high spectral resolution infrared observations, *IEEE Trans Geosci. Remote Sens.*, *42*, 842–853.

Hutchison, K. D., and K. R. Hardy (1995), Threshold functions for automated cloud analyses of global meteorological satellite imagery, *Int. J. Remote Sens.*, *16*, 3665–3680.

Hutchison, K. D., K. R. Hardy, and B.-C. Gao (1995), Improved detection of optically thin cirrus clouds in nighttime multispectral meteorological satellite imagery using total integrated water vapor information, *J. Appl. Meteorol.*, *34*, 1161–1168.

Inoue, T. (1985), On the temperature and effective emissivity determination of semi-transparent cirrus clouds by bi-spectral measurements in the 10 μm window region, *J. Meteorol. Soc. Jpn.*, *63*, 88–99.

Jensen, E., and L. Pfister (2004), Transport and freeze-drying in the tropical tropopause layer, *J. Geophys. Res.*, *109*, D02207, doi:10.1029/2003JD004022.

Kahn, B. H., A. Eldering, S. A. Clough, E. J. Fetzer, E. Fishbein, M. R. Gunson, S.-Y. Lee, P. F. Lester, and V. J. Realmuto (2003), Near micron-sized cirrus cloud particles in high-resolution infrared spectra: An orographic case study, *Geophys. Res. Lett.*, *30*(8), 1441, doi:10.1029/2003GL016909.

Kahn, B. H., A. Eldering, M. Ghil, S. Bordoni, and S. A. Clough (2004), Sensitivity analysis of cirrus cloud properties from high-resolution infrared spectra. Part I: Methodology and synthetic cirrus, *J. Clim.*, *17*, 4856–4870.

Lambrigtsen, B. H. (2003), Calibration of the AIRS microwave instruments, *IEEE Trans Geosci. Remote Sens.*, *41*, 369–378.

Lee, T. F., J. Turk, and K. Richardson (1997), Stratus and fog products using *GOES-8–9* 3.9 μm data, *Weather Forecast.*, *12*, 664–677.

Liou, K. N. (1986), Influence of cirrus clouds on weather and climate processes: A global perspective, *Mon. Weather Rev.*, *114*, 1167–1199.

Liou, K. N., Y. Takano, and P. Yang (2000), Light scattering and radiative transfer in ice crystal clouds: Applications to climate research, in *Light Scattering by Nonspherical Particles: Theory, Measurements and Geophysical Applications*. edited by M. I. Mishchenko, J. W. Hovenier, and L. D. Travis, pp. 417–449 Springer, New York.

Lutz, H.-J., T. Inoue, and J. Schmetz (2003), Comparison of a split-window and a multi-spectral cloud classification for MODIS observations, *J. Meteorol. Soc. Jpn.*, *81*, 623–631.

McFarquhar, G. M., A. J. Heymsfield, J. Spinhirne, and B. Hart (2000), Thin and subvisual tropopause tropical cirrus: Observations and radiative impacts, *J. Atmos. Sci.*, *57*, 1841–1853.

Mishchenko, M. I., and L. D. Travis (1998), Capabilities and limitations of a current Fortran implementation of the *T*-matrix method for randomly

oriented, rotationally symmetric scatterers, *J. Quant. Spectrosc. Radiat. Transfer*, *60*, 309–324.

Moncet, J. L., and S. A. Clough (1997), Accelerated monochromatic radiative transfer for scattering atmospheres: Application of a new model to spectral radiance observations, *J. Geophys. Res.*, *102*, 21,853–21,866.

Nasiri, S. L., and B. A. Baum (2004), Daytime multilayered cloud detection using multispectral imager data, *J. Atmos. Ocean. Technol.*, *21*, 1145–1155.

Ou, S. C., K. N. Liou, Y. Takano, N. X. Rao, Q. Fu, A. J. Heymsfield, L. M. Miloshevich, B. Baum, and S. A. Kinne (1995), Remote sounding of cirrus cloud optical depths and ice crystal sizes from AVHRR data: Verification using FIRE II IFO measurements, *J. Atmos. Sci.*, *52*, 4143–4158.

Ou, S. C., Y. Takano, K. N. Liou, G. J. Higgins, A. George, and R. Slonaker (2003), Remote sensing of cirrus cloud optical thickness and effective particle size for the National Polar-orbiting Operational Environmental Satellite System Visible/Infrared Imager Radiometer Suite: Sensitivity to instrument noise and uncertainties in environmental parameters, *Appl. Opt.*, *42*, 7202–7214.

Peter, T., et al. (2003), Ultrathin Tropical Tropopause Clouds (UTTCs): I. Cloud morphology and occurrence, *Atmos. Chem. Phys.*, *3*, 1083–1091.

Pierangelo, C., A. Chédin, S. Heilliette, N. Jacquinet-Husson, and R. Armante (2004), Dust altitude and infrared optical depth from AIRS, *Atmos. Chem. Phys.*, *4*, 1813–1822.

Platnick, S., M. D. King, S. A. Ackerman, W. P. Menzel, B. A. Baum, J. C. Riedl, and R. A. Frey (2003), The MODIS cloud products: Algorithms and examples from Terra, *IEEE Trans. Geosci. Remote Sens.*, *41*, 459–473.

Platt, C. M. R., S. A. Young, P. J. Manson, G. R. Patterson, S. C. Marsden, R. T. Austin, and J. H. Churnside (1998), The optical properties of equatorial cirrus from observations in the ARM pilot radiation observation experiment, *J. Atmos. Sci.*, *55*, 1977–1997.

Potter, G. L., and R. D. Cess (2004), Testing the impact of clouds on the radiation budgets of 19 atmospheric general circulation models, *J. Geophys. Res.*, *109*, D02106, doi:10.1029/2003JD004018.

Prabhakara, C., R. S. Fraser, G. Dalu, M.-L. C. Wu, and R. J. Curran (1988), Thin cirrus clouds: Seasonal distribution over oceans deduced from Nimbus-4 IRIS, *J. Appl. Meteorol.*, *27*, 379–399.

Prabhakara, C., D. P. Kratz, J.-M. Yoo, G. Dalu, and A. Vernekar (1993), Optically thin cirrus clouds: Radiative impact on the warm pool, *J. Quant. Spectrosc. Radiat. Transfer*, *49*, 467–483.

Rädel, G., C. J. Stubenrauch, R. Holz, and D. L. Mitchell (2003), Retrieval of effective ice crystal size in the infrared: Sensitivity study and global measurements from TIROS-N Operational Vertical Sounder, *J. Geophys. Res.*, *108*(D9), 4281, doi:10.1029/2002JD002801.

Randall, D. A., M. Khairoutdinov, A. Arakawa, and W. Grabowski (2003), Breaking the cloud parameterization deadlock, *Bull. Am. Meteorol. Soc.*, *84*, 1547–1564.

Rolland, P., and K. N. Liou (2001), Surface variability effects on the remote sensing of thin cirrus optical and microphysical properties, *J. Geophys. Res.*, *106*, 22,965–22,977.

Rolland, P., K. N. Liou, M. D. King, S. C. Tsay, and G. M. McFarquhar (2000), Remote sensing of optical and microphysical properties of cirrus clouds using Moderate-Resolution Imaging Spectroradiometer channels: Methodology and sensitivity to physical assumptions, *J. Geophys. Res.*, *105*, 1721–1738.

Roskovensky, J. K., and K. N. Liou (2003), Detection of thin cirrus from 1.38 μm/0.65 μm reflectance ratio combined with 8.6–11 μm brightness temperature difference, *Geophys. Res. Lett.*, *30*, 1985, doi:10.1029/2003GL018135.

Saunders, R. W., and K. T. Kriebel (1988), An improved method for detecting clear sky and cloudy radiances from AVHRR data, *Int. J. Remote Sens.*, *9*, 123–150.

Sherwood, S. C., and A. E. Dessler (2001), A model for transport across the tropical tropopause, *J. Atmos. Sci.*, *58*, 765–779.

Stephens, G. L. (2002), Cirrus, climate, and global change, in *Cirrus*, edited by D. K. Lynch et al., pp. 433–448, Oxford Univ. Press, New York.

Stephens, G. L., et al. (2002), The CloudSat mission and the A-train, *Bull. Am. Meteorol. Soc.*, *83*, 1771–1790.

Strabala, K. I., S. A. Ackerman, and W. P. Menzel (1994), Cloud properties inferred from 8–12 μm data, *J. Appl. Meteorol.*, *33*, 212–229.

Strow, L. L., S. E. Hannon, S. DeSouza-Machado, H. E. Motteler, and D. Tobin (2003), An overview of the AIRS radiative transfer model, *IEEE Trans. Geosci. Remote Sens.*, *41*, 303–313.

Susskind, J., C. D. Barnet, and J. M. Blaisdell (2003), Retrieval of atmospheric and surface parameters from AIRS/AMSU/HSB data in the presence of clouds, *IEEE Trans. Geosci. Remote Sens.*, *41*, 390–409.

Webster, P. J. (1994), The role of hydrological processes in ocean-atmosphere interactions, *Rev. Geophys.*, *32*, 427–476.

Wei, H., P. Yang, J. Li, B. A. Baum, H.-L. Huang, S. Platnick, Y. Hu, and L. Strow (2004), Retrieval of semitransparent ice cloud optical thickness from Atmospheric Infrared Sounder (AIRS) measurements, *IEEE Trans. Geosci. Remote Sens.*, *42*, 2254–2267.

Wu, X. Q., and W. L. Smith (1997), Emissivity of rough sea surface for 8–13 μm: Modeling and verification, *Appl. Opt.*, *36*, 2609–2619.

Wylie, D. P., and W. P. Menzel (1999), Eight years of high cloud statistics using HIRS, *J. Clim.*, *12*, 170–184.

Yang, P., and K. N. Liou (1996), Geometric-optics-integral-equation method for light scattering by nonspherical ice crystals, *Appl. Opt.*, *35*, 6568–6584.

Yang, P., K. N. Liou, K. Wyser, and D. Mitchell (2000), Parameterization of the scattering and absorption properties of individual ice crystals, *J. Geophys. Res.*, *105*, 4699–4718.

Yang, P., H. L. Wei, B. A. Baum, H. L. Huang, A. J. Heymsfield, Y. X. Hu, B. C. Gao, and D. D. Turner (2003), The spectral signature of mixed phase clouds composed of non-spherical ice crystals and spherical liquid droplets in the terrestrial window region, *J. Quant. Spectrosc. Radiat. Transfer*, *79*, 1171–1188.

Ziereis, H., et al. (2004), Uptake of reactive nitrogen on cirrus cloud particles during INCA, *Geophys. Res. Lett.*, *31*, L05115, doi:10.1029/2003GL018794.

S. DeSouza-Machado, S. E. Hannon, and L. L. Strow, Department of Physics, University of Maryland Baltimore, 1000 Hilltop Circle, Baltimore, MD 21250, USA.

A. Eldering, E. J. Fetzer, E. F. Fishbein, and S.-Y. Lee, Jet Propulsion Laboratory, 4800 Oak Grove Drive, Pasadena, CA 91109, USA.

B. H. Kahn and K. N. Liou, University of California at Los Angeles, Department of Atmospheric and Oceanic Sciences, 405 Hilgard Avenue, Box 951565, Los Angeles, CA 90095-1565, USA. (briank@atmos.ucla.edu)